Nature Communications

https://doi.org/10.1038/s41467-026-68775-9

Article in Press

Ultra-stretchable and crack-resistant nonpolar organogels

Received: 25 June 2025

Accepted: 15 January 2026

Cite this article as: Huang, Z., Peng, J., Zhang, W. *et al.* Ultra-stretchable and crack-resistant nonpolar organogels. *Nat Commun* (2026). https://doi.org/10.1038/s41467-026-68775-9

Zhenkai Huang, Jianping Peng, Wei Zhang, Kan Yue & Xun Wang

Ultra-stretchable and crack-resistant nonpolar organogels

Zhenkai Huang[1,2,†], Jianping Peng[1,3,†], Wei Zhang[1], Kan Yue[1*], Xun Wang[4*]

[1]State Key Lab of Luminescent Materials and Devices, Guangdong Provincial Key Laboratory of Functional and Intelligent Hybrid Materials and Devices, Guangdong Basic Research Center of Excellence for Energy and Information Polymer Materials, South China Advanced Institute for Soft Matter Science and Technology, School of Emergent Soft Matter, South China University of Technology, Guangzhou, China.

[2]School of Materials and Energy, Foshan University, Foshan, China.

[3]School of Environment and Chemical Engineering, Foshan University, Foshan, China.

[4]Engineering Research Center of Advanced Rare Earth Materials, Department of Chemistry, Institute of Tsinghua University (Hebei), Tsinghua University, Beijing, China.

*Corresponding author. Email: kanyue@scut.edu.cn (K.Y.); wangxun@mail.tsinghua.edu.cn (X.W.)

†These authors contributed equally to this work.

ABSTRACT

The inherent low polarity and weak intermolecular interactions of nonpolar media impose a fundamental thermodynamic constraint on gelation. Despite recent breakthroughs in designing highly stretchable and tough hydrogels, developing organogels that absorb nonpolar organic liquids with comparable mechanical performance has remained elusive. We report an ultra-stretchable and crack-resistant nonpolar organogel engineered through an inorganic nanowire-polymer hybrid network, overcoming the elasticity-strength trade-off. This hybrid network can absorb and gelate diverse nonpolar organic liquids at mass absorption ratios reaching over 35:1. The resultant organogels exhibit outstanding mechanical properties, including breaking elongation up to 1600% and true fracture strength over 1.5 MPa. In addition, through dynamic strain-induced nanowire alignment during tensile deformation, the organogels possess outstanding crack and fatigue resistance (fracture energy up to 1.7 kJ m^{-2} and fatigue threshold up to 95.3 J m^{-2}). These advances make our organogels ideal for nonpolar organic liquid solidification and spilled petrol recovery applications.

INTRODUCTION

Organogels, formed by immobilizing organic liquids within three-dimensional gelator networks[1,2], derive their multifunctionality from synergistic interactions between liquid and solid components[3-5]. Compared to hydrogels[6-9], organogels exhibit broader compatibility with diverse organic liquids as dispersion media and theoretically possess greater versatility for specialized applications[10-13]. However, to date organogels remain significantly underdeveloped[1,3,7]. This disparity originates from the intrinsically weak intermolecular interactions in organic liquids, particularly in nonpolar systems dominated by van der Waals forces[2,3,14-16], which pose a fundamental challenge in designing nonpolar organogels with mechanical robustness comparable to hydrogels[6,8,9] and thus might limit their practical applications due to insufficient mechanical properties[1,3,7].

Recent advances in inorganic nanowire gelators offer partial solutions[1,17-20]. These polymer-like nanowires, assembled from alkaline earth metal cations-bridged polyoxometalate (POM) clusters via electrostatic interactions, exhibit physical entanglement behaviors akin to polymer chains. At ultralow concentrations, they form a physically crosslinked network structure capable of immobilizing various nonpolar organic liquids[17,18]. While current nanowire-based organogels demonstrate moderate strength and stretchability, their structural tunability and surface ligand chemistry offer promising opportunities for optimization[19,20]. In particular, anchoring polymerizable ligands onto nanowires promise the construction of hybrid network architectures[21,22] that might transcend existing mechanical limitations in organogels. Paradoxically, despite the conceptual feasibility, experimental realization of nanowire-polymer hybrid organogel systems remains undocumented in the literature[1,4].

In this work, we develop an ultra-stretchable and crack-resistant nonpolar organogel through covalent integration of an inorganic nanowire network with an elastic polymeric network. This design moves beyond the traditional gelation paradigm driven by van der Waals forces[17,18],

introducing a covalent bonding polymer matrix that synergizes with the physical network. The entropy-driven elasticity of the polymer network allows for enhanced extensibility, while the energy-dissipative rigidity of the nanowires provides structural reinforcement and permits high fracture strength. Through this synergy, the hybrid network architecture delivers a striking enhancement in both stretchability (over 10-fold) and fracture strength (over 10-fold) compared to the reported nanowire-based organogels. Moreover, under tensile strain, the hybrid network dynamically reorients into an anisotropic architecture through nanowire alignment, thereby enabling outstanding crack and fatigue resistance in nonpolar organogels. This breakthrough bridges the long-standing mechanical performance gap between nonpolar organogels and reported polar gel systems.

Results

Inorganic Nanowire-Polymer Hybrid Network

It is well-documented that one-dimensional (1D) nanowires can be ingeniously formed through a dynamic adsorption-desorption equilibrium between nuclei and ligands[17-20]. After formation from precursors, the initial nuclei/clusters are rapidly capped by ligands. Further growth occurs only when the ligands desorb, exposing the cluster cores. The higher probability of ligand desorption from a single set of crystal faces compared to simultaneous desorption from multiple facets serves as the kinetic determinant for the formation of 1D nanowires[20]. To fabricate the hybrid nanowire-polymer network, a polymerizable ligand featuring an alkane carbon chain and a terminal amino group was designed to functionally mimic oleylamine, thereby enabling its partial replacement as a surface-capping agent (Fig. 1a). This ligand was engineered to bind to the nanowire surface via coordination and electrostatic interactions, thus introducing reactive acrylate groups to form polymerizable nanowires (PNWs, Fig. 1b). Furthermore, we postulated that PNW could be dispersed in a mixture of nonpolar organic solvents (*e.g.*, octane) and acrylate monomers (*e.g.*,

butyl acrylate, BA) to form physical organogels. Upon UV irradiation in the presence of a photoinitiator, *in situ* polymerization was expected to convert these physical organogels into PNW-polyacrylate hybrid organogels (Fig. 1c). Central to this design was the hypothesis that the entangled PNW-polymer hybrid network, featuring polymer chain-wrapped PNW bundles (Fig. 1d), would mechanically reinforce the hybrid organogels through the synergy of the rigidity of nanowires and flexibility of the polymer chains.

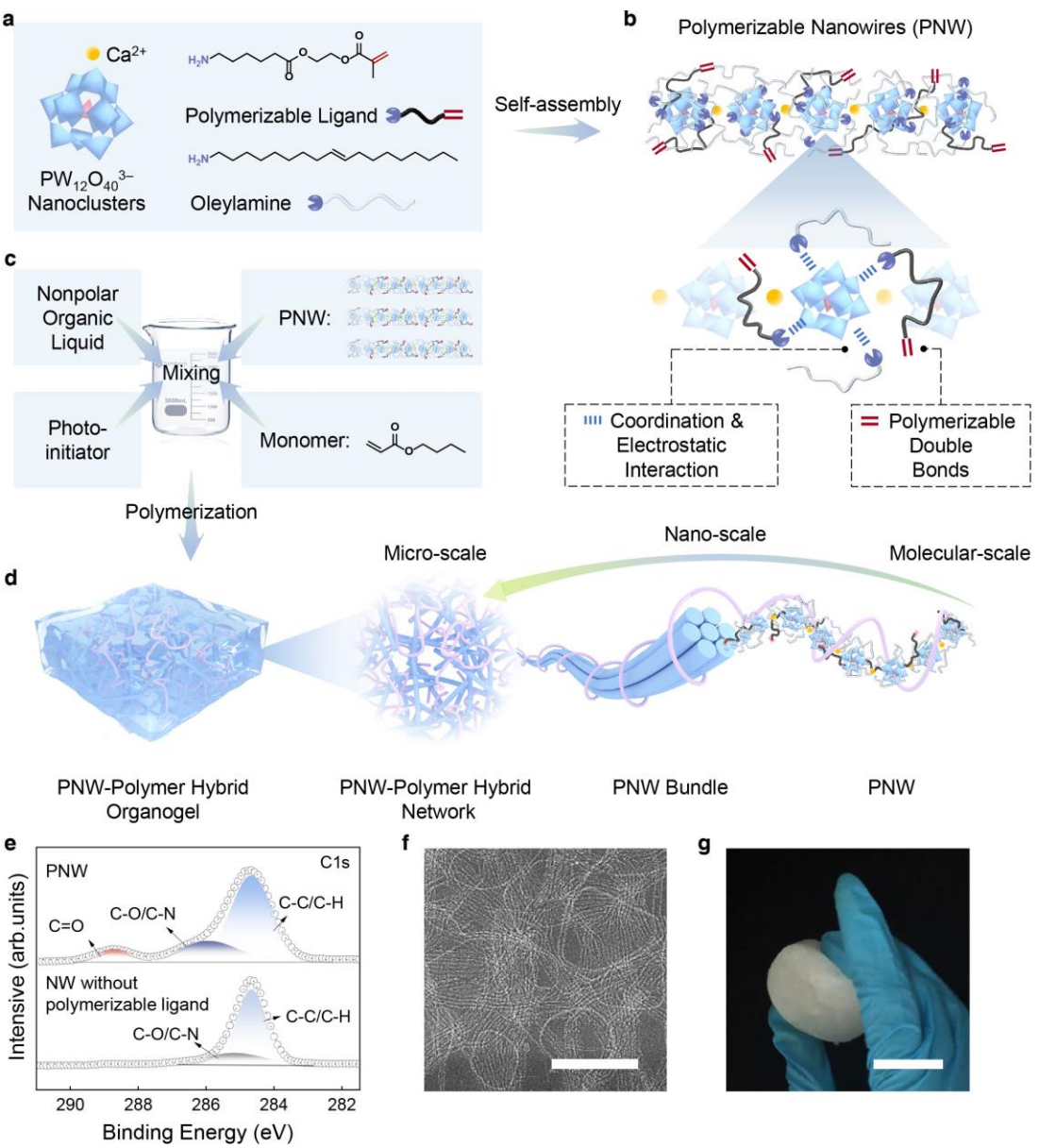

Fig. 1 | Design of the polymerizable PNWs and the Inorganic PNW-Polymer Hybrid Network. **a**, Chemical structures and schematic illustration of the self-assembly of Ca^{2+} and $PW_{12}O_{40}^{3-}$ with

two different ligands into PNWs. **b**, Schematic illustration of the PNWs with surface bonded oleylamines and polymerizable ligands through coordination and electrostatic interactions. **c**, One-step photoinitiated polymerization to obtain the PNW-polyacrylate hybrid network. **d**, Schematic illustration of the PNW-polymer hybrid network across multiple length scales. **e**, XPS spectra of PNWs and NWs without the polymerizable ligands. The emergence of an additional characteristic peak of the C=O bond indicates the successfully coordination of the polymerizable ligand onto the PNWs. **f**, TEM image of PNWs showing a densely stacked nanowire network. Scale bar: 100 nm. **g**, Optical photograph of a physical nonpolar organogel made from PNWs dispersed in octane. Scale bar: 3 cm.

To validate our design and hypotheses, we synthesized the polymerizable ligand as depicted in Supplementary Fig.1a, with its structure confirmed by ^{1}H and ^{13}C nuclear magnetic resonance (NMR) spectroscopy (Supplementary Fig. 1b,c). Using this polymerizable ligand and oleylamine, Ca^{2+} ions and $[PW_{12}O_{40}]^{3-}$ POMs can be assembled into PNWs (Fig. 1b) in a facile one-pot procedure[17,20]. Both the polymerizable ligand and oleylamine were expected to anchor on the PNW surface through electrostatic and coordination interactions to maintain charge neutrality of the nanowire[17]. Control nanowires with only oleylamine ligands (NWs) were prepared analogously (Supplementary Fig. 2a).

We performed X-ray photoelectron spectroscopy (XPS) analysis to confirm the elemental composition (Ca 2*p*, W 4*f*, P 2*p*, O 1*s*) in both nanowire samples (Supplementary Fig. 2d-h). Critically, the appearance of a C=O peak in the C 1s spectrum of PNW, absent in control NW, directly demonstrates the successful coordination of the polymerizable ligand to the $[PW_{12}O_{40}]^{3-}$ POM cluster (Fig. 1e). Notably, the slight blue shift in the C–O/C–N characteristic peak arises from the higher proportion of C–O bonds, which have a higher binding energy[23,24]. This finding is consistent with Fourier transform infrared (FT-IR) spectroscopy results (Supplementary Fig. 2i,j), where a distinct peak at 1738 cm^{-1}, corresponding to the C=O stretching vibration of the polymerizable ligand, is exclusively observed in PNW and absent in control NW synthesized solely with oleylamine. Dark-field transmission electron microscopy (TEM) imaging revealed that PNW (Fig. 1f) and control NW (Supplementary Fig. 2a) exhibited comparable curvilinear

nanostructures, confirming that ligand modification preserved the nanowire morphology, which is consistent with our previously study[17,20]. Moreover, the occassionally observed circular-shaped nanowires (Fig. 1f) suggests the polymer-like flexibility, enabling them to bend freely and even to curl into closed loops[17]. In addition, both types of nanowires effectively gelled organic solvents like octane (Fig. 1g and Supplementary Fig. 2b,c). The gelation of these physical organogels is driven by van der Waals interactions between alkyl chains on the nanowire surface ligands and the nonpolar organic liquid[17,20].

Mechanical Properties of the PNW-Polymer Organogels

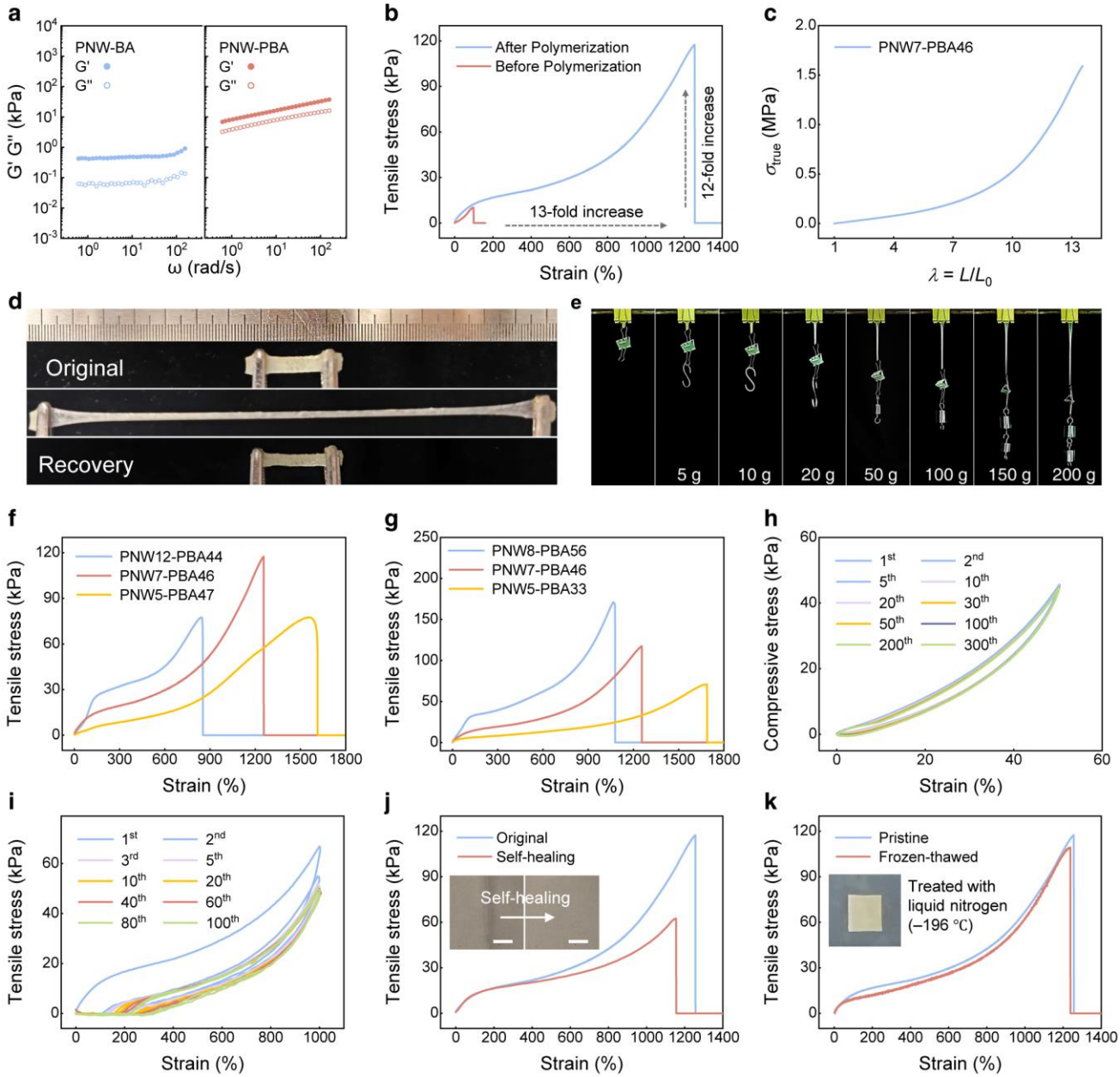

Fig. 2 | Mechanical properties of the PNW-PBA organogels. a, Rheological behaviors of the organogels before and after polymerization in the frequency sweep mode for a strain amplitude of 1%. **b**, Representative tensile stress-strain curves of the organogels before and after polymerization at strain rate of 100 mm min^{-1}. **c**, True tensile stress-strain curve of the PNW7-PBA46 organogel. **d**-**f**, Illustration of the (**d**) excellent stretchability under stretching and (**e**) mechanical strength with increasing loads of the PNW7-PBA46 organogel. **f**, Tensile stress-strain curves of the PNW5-PBA47, PNW7-PBA46, and PNW12-PBA44 organogels with different PNW mass fractions. **g**, Tensile stress-strain curves of the PNW8-PBA56, PNW7-PBA46, and PNW5-PBA33 organogels with different octane contents. **h**, 300 cycles of compressive stress-strain curves of the PNW7-PBA46 organogel at 50% strain. **i**, Cyclic tensile curves of the PNW7-PBA46 organogel under a strain of 1000%. **j**, Comparison of the stress-strain curves of the original and self-healed PNW7-PBA46 organogels. Inset: Optical micrographs of a cut PNW7-PBA46 organogel before and after healing under ambient conditions for 24 h. **k**, Stress-strain curves of the PNW7-PBA46 organogel

in the original state and after freeze-thaw treatment with liquid nitrogen. Inset: Optical micrograph of an undamaged PNW7-PBA46 organogel strip treated with liquid nitrogen.

We observe that the PNWs with surface acrylate groups can also be dispersed at a range of mass fraction (up to 12.0 wt%) in the 1:1 (m/m) mixture of BA and octane, forming physical PNW-BA-octane organogels (Supplementary Fig. 3a). Take a representative formulation of of 7.0 wt% PNWs, 46.0 wt% PBA, and 47.0 wt% octane as the example, the formation of a physical organogel is validated from rheological characterization. In the frequency sweep at a strain amplitude of 1%, the energy storage modulus (G') of the organogels was consistently higher than the loss modulus (G'') throughout the angular velocity range of the rheological test, confirming that the organogels behave as typical elastomers throughout the frequency range (Fig. 2a)[2,7]. Furthermore, G' showed a gradual increase with increasing ω, indicating that the organogels displayed greater elasticity than viscosity. Previous studies have revealed that the elastic properties of the nanowire-based organogels are attributed to the physical crosslinking between the nanowire network, caused by the nanowire entanglements[17]. Moreover, the concurrent significant rise in G'' reflects the enhanced energy dissipation capability inherent to this hybrid architecture, while the increased frequency dependence of G'' after polymerization is another evidence of the successful transition to a complex hybrid network with rich relaxation processes[7]. At low frequencies, the flexible PBA chains have sufficient time to relax and reconfigure, dissipating energy. At high frequencies, these dynamics are constrained, causing the network to appear stiffer. This rheological signature is fully consistent with the observed orders-of-magnitude improvement in modulus.

UV-initiated *in situ* polymerization of BA converted the physical organogel into a hybrid matrix composed of both PNW and poly(butyl acrylate) (PBA) networks (refer to the Supplementary Note 1 in the Supplementary Information for details). The PBA network is chemically crosslinked to the PNW network through the polymerizable ligands, resulting in a PNW-polymer hybrid network swollen by residue octane (Supplementary Fig. 3a-d). Notably,

during the polymerization, the PNWs and bundles remain intact, since the SAXS profiles show identical scattering peak attributed to the nanowire bundles before and after polymerization (Supplementary Fig. 3e). During polymerization, the polymerizable ligands bound to the PNW surface copolymerize with BA monomers, thereby bonding the PNW to the polymer network (Supplementary Fig. 3f). Specifically, this organogel is referred as the **PNW7-PBA46** organogel. To examine the microstructure of the PNW-PBA organogel, we performed TEM imaging of cryo-ultrathin sections of the PNW-PBA hybrid network. As shown in Supplementary Fig. 3g, the nanowires maintain their structural integrity and remain well-dispersed within the polymer matrix, which is consistent with the TEM image of PNW dispersed in octane (Fig. 1f), and reinforce the organogel through cross-linking with the polymer network. Owing to its weak electron-scattering capability, the polymer matrix appears as a light grey background with nebulous morphology under TEM (Supplementary Fig. 3g). Distinctly different rheological behaviors (Fig. 2a) evidence the polymerization-induced transition from physical to chemical cross-linking. We observe that the PNWs with surface acrylate groups can also be dispersed at a range of mass fraction (up to 12.0 wt%) in the 1:1 (m/m) mixture of BA and octane, forming physical PNW-BA-octane organogels (Supplementary Fig. 3a). Notably, the PNWs remain the bundled nanowire structure as revealed by the almost identical TEM images (Supplementary Fig. 3h) and SAXS profiles (Supplementary Fig. 3e). The near-100-fold increase in *G*' post-polymerization signifies the formation of a robust, elastic hybrid network via chemical crosslinking between the PBA and PNW networks (Fig. 2a)[25]. Prepared from the identical protocol, the control NW-PBA-octane organogel without polymerizable ligand exhibited insufficient mechanical strength to be self-supporting (Supplementary Fig. 3i-k). The control NW-PBA-octane organogel and PNW-PBA-octane organogel differed only by the presence of the polymerizable ligand, yet exhibited orders-of-magnitude differences in mechanical properties (Fig. 2a-e, and Supplementary Fig. 3i-k). This

stark contrast validates the successful hybridization of the PNW network and the PBA network through the polymerizable ligands. Such a hybrid PNW-PBA network, along with nanowire entanglement and van der Waals interactions between the nanowire ligands and the organic liquid, collectively drives the gelation of our nonpolar organogel.

We used Fourier transform infrared (FT-IR) spectroscopy to monitor the polymerization (Supplementary Fig. 3l,m). Characteristic peaks of the $[PW_{12}O_{40}]^{3-}$ POM cluster (948 cm^{-1}) and the out-of-plane bending vibrations of C-H bond in oleylamine (~760 cm^{-1}) persisted post-polymerization; while the disappearance of the C=C bond stretching vibration at ~1630 cm^{-1} was observed, accompanied by a 4 cm^{-1} shift in the carbonyl stretching vibration (C=O) of the PBA matrix from 1730 to 1734 cm^{-1}. The complete conversion of BA monomer was also verified by ^{1}H NMR spectroscopy (Supplementary Fig. 3n). After polymerization, the resonance peaks assigned to protons of the unsaturated C=C bonds at δ 6.38, 6.11, 5.80, and 4.15 ppm disappeared, while new peaks at δ 4.04, 2.27, and 1.90 ppm emerged, indicating successful polymerization of the BA monomer into PBA.

We tested the mechanical performance of the as-prepared PNW7-PBA46 organogel via a uniaxial tensile experiment. Before polymerization, the breaking elongation of the precursor physical organogel is ~100% (Fig. 2b). In contrast, the PNW7-PBA46 organogel demonstrated pronouncedly enhanced stretchability and tensile strength (both over 10-fold). The combination of high fracture strength (117.4 kPa) and stretchability (>1,200%) of the PNW7-PBA46 organogel represents outstanding metrics in reported nonpolar organogels. True stress-strain analysis revealed exceptional strain-stiffening behavior. The peak true strength of PNW7-PBA46 organogel reached 1.5 MPa (Fig. 2c), and its differential modulus exhibited a 17-fold increase at maximum strain (Supplementary Fig. 4a). The excellent mechanical properties of the PNW7-PBA46 organogel was visually illustrated by a reversible stretching of a strip sample to 10 times

its original length, which fully recovered upon releasing the tensile stress (Fig. 2d and Supplementary Movie 1). Moreover, a PNW7-PBA46 organogel strip ($10 \times 5 \times 1.5\ mm^3$ in size) supported up to 200-g loads without rupture (Fig. 2e), demonstrating the effectiveness of our hybrid network reinforcement.

We speculate that the concurrent enhancement of stretchability and fracture strength stems from the complementary roles of the inorganic nanowires and the polymer network. The rigid nanowires act as sacrificial stress-concentrating units that redistribute localized strains, delaying crack initiation[7,11]. Meanwhile, the flexible polymer chains dissipate energy through reversible chain entanglement and bond reconfiguration during elongation[9]. This hybrid architecture thereby overcomes the conventional stretchability-strength trade-off by allowing substantial energy absorption via polymer chain flexibility while maintaining structural integrity through nanowire-mediated stress transfer[22]. Impressively, this hybrid reinforcement results in an over 100-fold improvement in toughness (524.0 kJ m^{-3} versus 4.6 kJ m^{-3}) of the organogels, which confirms the hybrid network formation and validates our hypothesis on the mechanical strengthening via the hybrid network design (Fig. 1d).

To tune the mechanical properties of the PNW-PBA-octane organogels, we modulated the mass ratios of PNW, PBA, and octane (refer to the Supplementary Note 2 in the Supplementary Information for details). Initial studies focused on PNW content variation (5.0-12.0 wt%) while maintaining a fixed 1:1 octane-to-BA ratio (m/m, Supplementary Table 1). Tensile testing revealed that as the PNW concentration increased from 5.0 wt% to 12.0 wt%, the ultimate strength initially rose from 77.4 kPa to 117.4 kPa, followed by a subsequent decrease back to 77.1 kPa, while the maximum extensibility consistently decreased from 1600% to 850% strain (Fig. 2f). This variation indicates that increased chemical crosslinking restricts the mobility of PBA chains yet reinforces the hybrid network. The influence of chemical crosslinking density was further probed by tuning

the content of the polymerizable ligand in PNW synthesis. At the same PNW content, a higher polymerizable ligand concentration resulted in elevated tensile stress coupled with reduced ductility (Supplementary Fig. 4b, and Supplementary Table 2). Moreover, as the octane content increased from 36.0 wt% to 62.0 wt%, the stretchability of the PNW-PBA-octane organogels improved while the strength decreased (Fig. 2g and Supplementary Table 3), likely due to the plasticization effect of octane[5,14].

The hybrid network confers notable resilience. Cyclic compression test (300 cycles at 50% strain) on PNW7-PBA46 organogel exhibited only a 2% drop in compressive stress after the first 5 cycles and remained almost unchanged during the subsequent 295 compression cycles (Fig. 2h and Supplementary Fig. 4c). In addition, the cyclic tensile test at 1000% strain on the PNW7-PBA46 organogel revealed 72% stress retention after 100 cycles (Fig. 2i and Supplementary Fig. 4d). This result suggests significant improvement of the PNW-PBA-octane organogels on the resistance to large cyclic deformation, far exceeding that of nonpolar organogels achieved by physical crosslinking of the nanowire network alone (Fig. 1g and Supplementary Fig. 2b). This enhancement stems from the synergistic energy dissipation mechanism. The chemically crosslinked polymer network stores elastic energy, while the entangled rigid PNW network enables structural recovery[7,9,26].

Interestingly, the PNW-PBA hybrid network also enables autonomous fracture repair. A severed PNW7-PBA46 organogel sample recovered 53% of the original fracture strength and 91% of the original breaking strain after healing in ambient conditions for 24 h (Fig. 2j), with optical microscopy showing near-complete crack closure (inset). We attribute this partial healing to the re-entanglement of the PBA chains. The DSC results indicate that the glass transition (T_g) of the PNW7-PBA46 hybrid network occurs at –36.8 °C (Supplementary Fig. 4e). The network therefore exhibits significant flexibility at room temperature, which facilitates sufficient molecular thermal

motion and permits re-entanglement[27], therefore enabling partial sell-healing of the organogel at room temperature (Fig. 2j). Moreover, the organogel maintained mechanical integrity after the freezing-thawing treatment in liquid nitrogen (Fig. 2k and Supplementary Fig. 4f-i), exhibiting almost identical stress-strain profiles before- and post-thawing. This cryogenic stability underscores the robustness of the hybrid network across extreme thermal conditions.

Strain-induced Alignment of Nanowires Enables Fatigue Resistance

We conducted small-angle X-ray scattering (SAXS) and scanning electron microscopy (SEM) experiments to probe the dynamic structural evolution of the strain-induced alignment of the PNW-PBA network (Fig. 3a). In the initial state (0% strain), 2D SAXS patterns of PNW7-PBA46 organogel exhibited an isotropic circle profile with uniform azimuthal intensity, and SEM imaging revealed isotropic surface morphology (Fig. 3b), indicating a random and uniform distribution of the PNW7-PBA46 network. The Herman's orientation factor (f) and degree of orientation (Π) were calculated through azimuthal integration of the 2D SAXS patterns (refer to the Supplementary Note 3 in the Supplementary Information for details)[11,25,28-29]. At 0% strain, the integration results were equivalent across all azimuths, yielding an f value close to zero (f = 0.070). As tensile strain increased from 0% to 800%, the 2D SAXS patterns exhibited intensity reduction along the vertical axis (parallel to the tensile direction with azimuthal angles of 0° and 180°), with enhanced scattering near the 90°/270° azimuths (Fig. 3c-f). This evolution signifies stress-induced nanowire alignment parallel to the tensile direction.

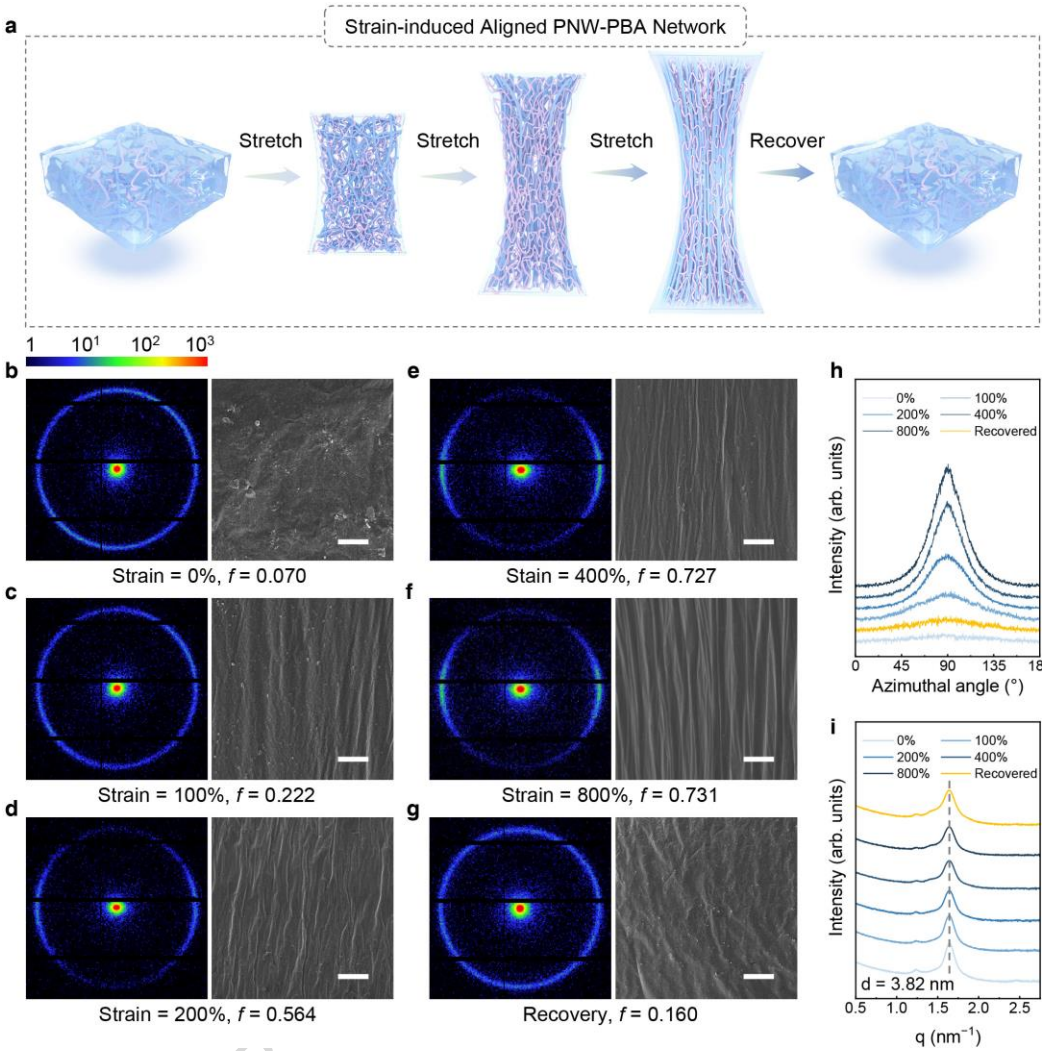

Fig. 3 | Strain-induced alignment of the PNW-PBA hybrid network. a, Schematic illustration of PNW alignment within the PNW-PBA hybrid network, depicting a random orientation in the pristine and recovered states and an aligned configuration under tensile strain. **b-g**, 2D SAXS patterns and corresponding SEM images of the PNW7-PBA46 organogels: **b-f**, under progressively increasing tensile strain and (**g**) after recovery. The Herman's orientation factor *f* is calculated from the azimuthal integration of 2D SAXS patterns. SEM images at different tensile strains clearly reveal the alignment of the PNW-PBA network, consistent with SAXS observations. Scale bar: 10 μm. **h**, Azimuthally integrated 1D SAXS curves derived from 2D SAXS patterns at varying tensile strains. A sharp increase in orientation is indicated by the pronounced peak at 90° under high tensile strain (blue curves). The post-recovery azimuthal integration curve (yellow) confirms the restoration of the PNW-PBA network. **i**, 1D SAXS profiles extracted from 2D SAXS patterns of PNW7-PBA46 organogels at different applied strains and after recovery, demonstrating an unchanged correlation length (d = 3.82 nm).

Azimuthal integration of 2D SAXS patterns at varying tensile strains and after recovery quantified this structural reorganization (Fig. 3h). The Herman's orientation factor *f* increases from 0.070 to 0.731 (where 0 denotes fully random distribution and 1 denotes perfect alignment) as the

tensile strain increases from 0% to 800%, with degree of orientation Π increases from 0.606 to 0.807, demonstrating a clear correlation between tensile strain and structural anisotropy of the PNW-PBA network. SEM imaging offers direct confirmation of strain-induced alignment, revealing a progressive orientation of the organogel surface along the tensile direction. Notably, upon stress release followed by a 5-minute recovery, the orientation of PNW-PBA hybrid network demonstrated rapid reversibility (Fig. 3g). The 2D SAXS pattern reverted to an almost isotropic circle, accompanied by a sharp decrease in f to 0.160 (Fig. 3h), while SEM images directly visualized this dynamic process with recovered random orientations post-relaxation. Collectively, these observations provide conclusive evidence for the reversible strain-induced alignment of the hybrid network under tensile strain.

Further structural analysis was conducted through 1D SAXS profiles derived from the integration of 2D SAXS patterns at varying tensile strains (0% to 800%) and during recovery (Fig. 3i). Applying the Bragg equation ($d = 2\pi/q_{max}$), the correlation length of the PNW7-PBA46 organogel was calculated from the scattering vector at the peak position (q_{max}). A prominent peak at $q = 1.64$ nm^{-1} corresponded to an inter-nanowire distance of $d = 3.82$ nm, consistent with our previous results[17,20]. The SAXS profiles indicating that while the PNW-PBA network aligned during stretching, the inter-nanowire distance remained unchanged. This non-correlated relationship suggests that PNW initially form parallel bundles (Fig. 1d), which subsequently undergo reversible orientation with increasing strain (Fig. 3a). Experimentally, the formation of bundles can be visualized in the TEM images (as shown in Supplementary Fig. 3h). SAXS data also confirms the average distance between neighboring nanowires within a bundle to be 3.82 nm (Fig. 3i). To assess nanowire stability during PNW-PBA hybrid network formation, SAXS profiles of PNW under various states were compared (Supplementary Fig. 3e). The inter-nanowire distance, measured as 3.87 nm in the PNW-octane organogel by SAXS, remained consistent after adding

acrylate monomers to form the PNW-BA-octane organogel, and was nearly identical (3.82 nm) in the final polymerized PNW-PBA organogel. These SAXS results confirm the stability of inter-nanowire spacing throughout hybrid network formation. Moreover, TEM imaging verified the consistent presence of individual nanowires and bundles across all stages of PNW-PBA network assembly (Fig. 1f, and Supplementary Fig. 3g-h).

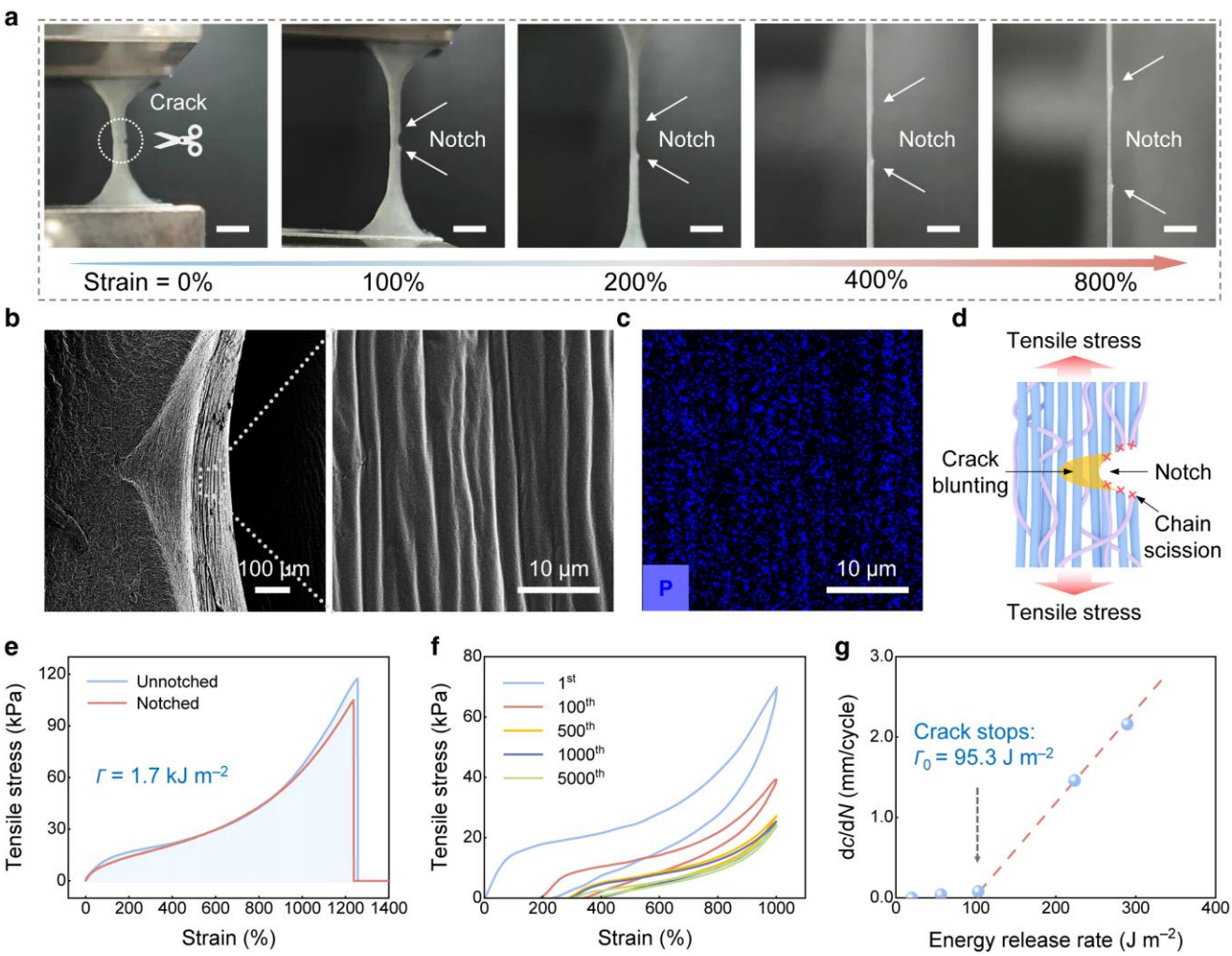

Fig. 4 | Crack and fatigue resistance of the PNW7-PBA46 organogel. a, Photographs of a notched PNW7-PBA46 organogel strip under increasing tensile strain Scale bars: 5 mm. As the strain increases, the pre-applied notch of the organogel fails to grow in the radial direction. **b**, SEM images with different magnifications and (**c**) EDS mapping image of the fracture of the organogel. A dense oriented arrangement of the PNW bundle structure was clearly observed at the fracture surface. **d**, Schematic illustration demonstrating that the alignment of the PNW-polymer hybrid network endows the nonpolar organogels with crack and fatigue resistance. **e** Nominal stress-strain curves of unnotched and notched PNW7-PBA46 organogels. The fracture energy (Γ) of the PNW7-PBA46 organogel is calculated to be 1.7 kJ m^{-2}. **f**, Cyclic tensile curves of a notched

PNW7-PBA46 organogel at 1000%. **g**, Crack extension per loading cycle, d*c*/d*N*, versus energy release rate for the PNW7-PBA46 organogel. The calculated fatigue threshold (Γ_0) was 95.3 J m^{-2}.

The reversible strain-induced alignment of the PNW-PBA hybrid network endows the organogel with exceptional crack-resistant properties. The pre-notched PNW7-PBA46 organogel exhibited excellent resistance to crack propagation during stretching, exhibiting a maximum breaking strain of over 1200% (Fig. 4a and Supplementary Movie 2). The correlation between the hybrid network and the crack resistance was demonstrated by SEM observation of the microstructure at the fracture site of the organogel (Fig. 4b). EDS mapping of phosphorus element distribution further revealed strain-induced alignment within the PNW-PBA hybrid network (Fig. 4c and Supplementary Fig. 5a-c). The pronounced strain-induced alignment of PNW-PBA hybrid network and the densification of aligned nanowires at the crack tip effectively prevented microcracks from propagating in the radical direction (Fig. 4d), thereby introducing unrecorded crack resistance in nonpolar organogels[1,4,5]. Using the single-edge notch tension (SENT) method (refer to the Supplementary Note 4 in the Supplementary Information for details), the fracture energy (Γ) of the PNW7-PBA46 organogel was calculated to be as high as 1.7 kJ m^{-2} (Fig. 4e), comparable to that of human skin (1.7-2.6 kJ m^{-2})[22]. Impressively, the pre-notched PNW5-PBA33 organogel sample with saturated octane content also retained crack-resistant properties (Supplementary Fig. 5d), validating the excellent toughness of the designed PNW-PBA hybrid network.

The dynamic reorganization of the nanowire-polymer hybrid network under large tensile strain provides an anitropic structural basis for fracture resistance. The aligned nanowires create tortuous crack propagation paths perpendicular to the stretching direction[6,30]. Crack tips are repeatedly pinned and bifurcated at nanowire-polymer interfaces, requiring substantially higher energy expenditure for crack advancement[7,11]. To quantify the fatigue resistance, we measured the fatigue threshold Γ_0 of the PNW7-PBA46 organogel via cyclic tensile tests conducted on pre-

notched samples (refer to the Supplementary Note 5 in the Supplementary Information for details)[6,22,30-33]. The pre-notched PNW7-PBA46 organogels resisted 5000 tensile cycles of less than 1000% strain without notable crack growth (Fig. 4f and Supplementary Fig. 5e). However, with increasing cyclic strain (strain = 1200%), the PNW7-PBA46 organogel fractured after 742 strain-release cycles (Supplementary Fig. 5f). This indicates that the energy applied to the organogel by this strain exceeded the fatigue threshold, causing the crack to grow rapidly. The calculated fatigue threshold Γ_0 of PNW7-PBA46 organogel is about 95.3 J m^{-2} (Fig. 4g).

To the best of our knowledge, the nonpolar organogel with a PNW-PBA hybrid network exhibits both crack and fatigue resistance, a combination which has not been previously reported for such materials. In contrast, although several nonpolar organogel systems have been previously reported with gelators including LMOG[3], polymer[14], and nanowire[17,18], none of them exhibit the combination of three desired properties, namely, mechanical robustness, self-healing capacity, and resistance to crack and fatigue (see Supplementary Table 4 for details). Furthermore, our ultra-stretchable and crack-resistant nonpolar organogels were compared with conventional polar organogels (see Supplementary Table 5 for details). This comparison reveals that our nonpolar organogels successfully bridge the long-standing mechanical performance gap between nonpolar organogels and reported polar organogel systems.

Absorption of Organic Liquids and Spilled Petrol Recovery

To tackle the challenge of gelating nonpolar organic liquids, we showed that the PNW-PBA hybrid network exhibits universal absorption capacity for a variety of nonpolar organic solvents (Fig. 5a and Supplementary Fig. 6a), forming freestanding organogels with solvent-dependent maximum absorption ratios (Fig. 5b). We briefly evaluated the absorption behaviors of the PNW-PBA hybrid network in a few common organic liquids, covering (cyclo)alkanes, (cyclo)alkenes, aromatic compounds, and commercial petrol (as a mixture of hydrocarbons). Specifically, the dried PNW7-

PBA46 sample displays excellent absorption performance with maximum swelling ratios of 38 times in anisole, 33 times in toluene, 32 times in xylene, and 24 times in petrol (commercial 92# petrol in China). This high absorption capacity consequently enhances the transparency of organogels, depending on the selection of the organic liquid (Fig. 5b and Supplementary Fig. 6b). From these results, it appears that the PNW-PBA hybrid network swells more in aromatic solvents than in aliphatic solvents, and the presence of unsaturated C=C bonds in organic solvents also contributes to a high swelling ratio. Comparison of the swelling behavior among the selected *n*-alkanes and cycloalkanes suggests the absorption preference of the PNW-PBA hybrid network for smaller *n*-alkanes and conformationally more compact cycloalkanes.

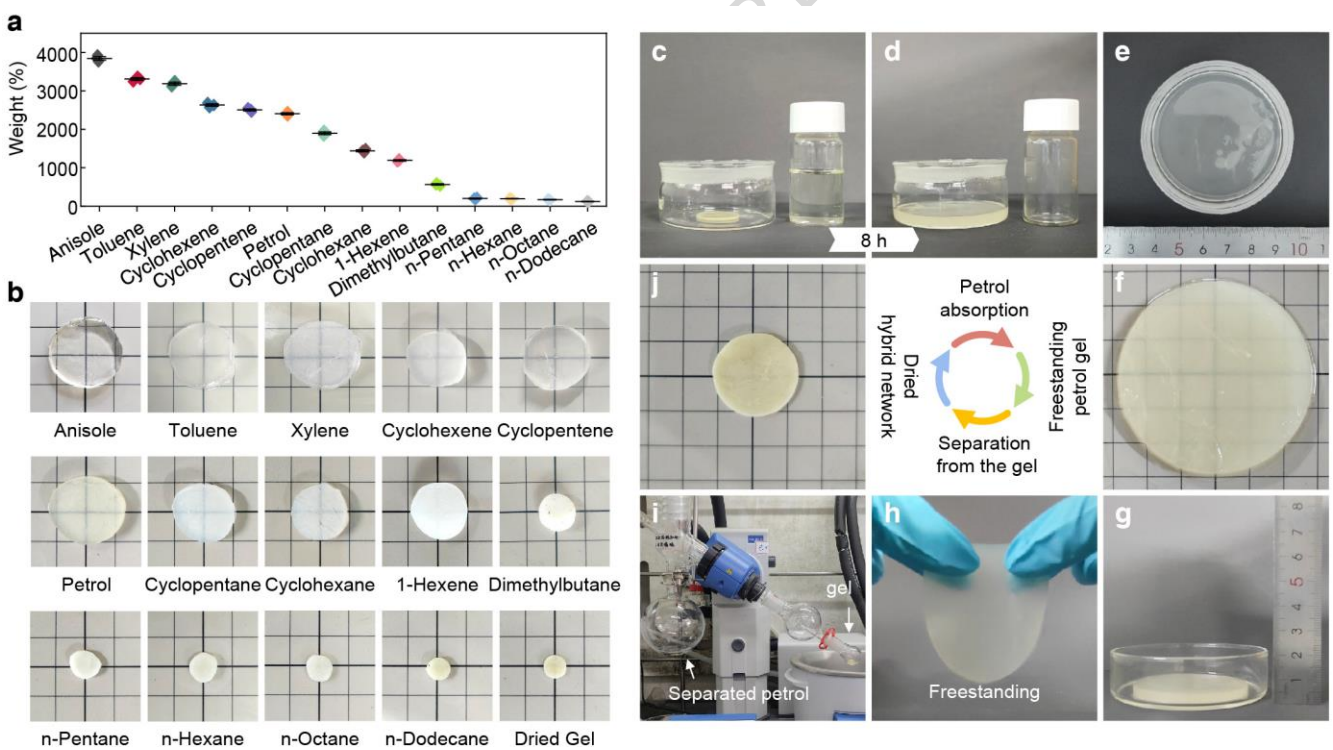

Fig. 5 | Organic liquid absorption and spilled petrol recovery performance of the PNW7-PBA46 organogel. a, Swelling ratios of the dried PNW7-PBA46 organogel in diverse nonpolar organic liquids, error bars represent the standard deviation of data within each group. **b**, Optical photograph of the organogel after equilibrium swelling in corresponding solvents. **c-j**, Sequential demonstration of petrol spill recovery using the PNW7-PBA46 organogel. The dried organogel exhibits excellent petrol absorption capacity, achieving a 3-fold diameter expansion and 24-fold mass increase. Petrol recovery is realized through reduced-pressure distillation, and the regenerated organogel maintains stable absorption performance over 10 reuse cycles.

Comparative study on a PNW-based hybrid network with an alternative poly(hexyl acrylate) (PHA) polymer revealed reduced absorption capacities compared with the PNW-PBA network (Supplementary Fig. 6c), indicating the critical role of polymer composition (refer to the Supplementary Note 6 in the Supplementary Information for details). Another set of control group organogels consisting solely of the PBA network (PBA organogels) showed marked decrease in absorption capacity for various nonpolar organic solvents (Supplementary Fig. 6d,e), underscoring the indispensable role of the PNW network in enabling high solvent uptake (refer to the Supplementary Note 7 in the Supplementary Information for details). The comparisons confirm the distinct capacity of the PNW-PBA network to synergistically combine nanowire-mediated solvent entrapment with the polymer matrix, establishing a generalized design platform for high-performance nonpolar organogels.

The absorption capacity and outstanding mechanical robustness of our PNW-PBA hybrid network facilitate practically viable spilled petrol recovery application, where the solidified petrol organogels would maintain structural integrity for facile handling. As a proof-of-concept demonstration, a dried PNW7-PBA46 organogel (Fig. 5c) was immersed in petrol to achieve equilibrium swelling (Fig. 5d), resulting in a 3-fold dimensional expansion and a 24-fold mass increase (Fig. 5e-g). Importantly, the swollen petrol organogel can be lifted as a freestanding film and transported without disintegration (Fig. 5h and Supplementary Movie 3). Although the fully swollen petrol organogel exhibited marked reduction in G' and G'' compared to the PNW7-PBA46 organogel in octane (Supplementary Fig. 6f), it could be stretched to over 200% in tensile test (Supplementary Fig. 6g), demonstrating the exceptional mechanical performance of the PNW-PBA hybrid network. Subsequently, petrol can be efficiently recovered from the organogel through distillation under reduced pressure (Fig. 5i). The dried organogel can then be reused for petrol absorption (Fig. 5j). This absorption-recovery cycle remained effective through at least 10

consecutive trials, demonstrating exceptional reusability and potential for environmental remediation application in oil spills.

Discussion

We demonstrated a mechanically robust and ultra-stretchable nonpolar organogel by leveraging an inorganic nanowire-polymer hybrid network. A polymerizable ligand was synthesized to chemically tether polymer chains to nanowires, which is a critical design for the hybrid network formation. The gelation and reinforcement mechanism is a synergistic combination: the initial immobilization of nonpolar solvents is achieved through van der Waals interactions with the nanowire network, while the outstanding mechanical robustness stems from the covalent integration of the rigid nanowire network with the flexible polymer matrix. The strain-induced alignment of the nanowire-polymer hybrid network effectively prevents cracks from propagating, resulting in an outstanding level of crack and fatigue resistance in nonpolar organogels. Furthermore, the organogels display notable self-healing properties, along with low-temperature resistance and the capacity for absorption of various nonpolar organic liquids. Collectively, these intriguing features impart to the organogels great potential for use in spilled petrol recovery. The strategy of hybrid network reinforcement can be potentially extended to other nonpolar gel materials with outstanding properties for various applications.

Data availability

All data generated or analysed during this study are included in this paper and the Supplementary Information. Data that support the findings of this study are available from the corresponding author upon request.

References

1 Zhang, S. & Wang, X. Inorganic Subnanometer Nanowire-Based Organogels: Trends, Challenges, and Opportunities. *ACS Nano* **17**, 20-26, (2023).

2 Lan, Y., Corradini, M. G., Weiss, R. G., Raghavan, S. R. & Rogers, M. A. To gel or not to gel: correlating molecular gelation with solvent parameters. *Chem. Soc. Rev.* **44**, 6035-6058, (2015).

3 Suzuki, M. & Hanabusa, K. Polymer organogelators that make supramolecular organogels through physical cross-linking and self-assembly. *Chem. Soc. Rev.* **39**, 455-463, (2010).

4 Kuzina, M. A., Kartsev, D. D., Stratonovich, A. V. & Levkin, P. A. Organogels versus Hydrogels: Advantages, Challenges, and Applications. *Adv. Funct. Mater.* **33**, 2301421, (2023).

5 Zeng, L. *et al.* Recent advances of organogels: from fabrications and functions to applications. *Prog. Org. Coat.* **159**, 106417, (2021).

6 Hua, M. *et al.* Strong tough hydrogels via the synergy of freeze-casting and salting out. *Nature* **590**, 594-599, (2021).

7 Li, X. & Gong, J. P. Design principles for strong and tough hydrogels. *Nat. Rev. Mater.* **9**, 380-398, (2024).

8 Chen, L. *et al.* A hyperelastic hydrogel with an ultralarge reversible biaxial strain. *Science* **383**, 1455-1461, (2024).

9 Kim, J., Zhang, G., Shi, M. & Suo, Z. Fracture, fatigue, and friction of polymers in which entanglements greatly outnumber cross-links. *Science* **374**, 212-216, (2021).

10. Zhao, Y. *et al.* A self-healing electrically conductive organogel composite. *Nat. Electron.* **6**, 206-215, (2023).

11. Li, W. *et al.* Nanoconfined polymerization limits crack propagation in hysteresis-free gels. *Nat. Mater.* **23**, 131-138, (2024).

12. Slavík, P., Trowse, B. R., O'Brien, P. & Smith, D. K. Organogel delivery vehicles for the stabilization of organolithium reagents. *Nat. Chem.* **15**, 319-325, (2023).

13. Lv, J., Yao, X., Zheng, Y., Wang, J. & Jiang, L. Antiadhesion Organogel Materials: From Liquid to Solid. *Adv. Mater.* **29**, 1703032, (2017).

14. Park, J.-M. *et al.* Aromatic nonpolar organogels for efficient and stable perovskite green emitters. *Nat. Commun.* **11**, 4638, (2020).

15. Urata, C., Nagashima, H., Hatton, B. D. & Hozumi, A. Transparent Organogel Films Showing Extremely Efficient and Durable Anti-Icing Performance. *ACS Appl. Mater. Interfaces* **13**, 28925-28937, (2021).

16. Yao, X. *et al.* Self-Replenishable Anti-Waxing Organogel Materials. *Angew. Chem. Int. Ed.* **54**, 8975-8979, (2015).

17. Zhang, S., Shi, W. & Wang, X. Locking volatile organic molecules by subnanometer inorganic nanowire-based organogels. *Science* **377**, 100-104, (2022).

18. Zhang, F., Li, Z. & Wang, X. Mechanically tunable organogels from highly charged polyoxometalate clusters loaded with fluorescent dyes. *Nat. Commun.* **14**, 8327, (2023).

19. Shi, Y., Shi, W., Zhang, S. & Wang, X. Revealing the Flexibility of Inorganic Sub-Nanowires by Single-Molecule Force Spectroscopy. *CCS Chem.* **5**, 2956-2965, (2023).

20. Liu, Q., Wang, X. & Wang, X. Sub-1 nm Materials Chemistry: Challenges and Prospects. *J. Am. Chem. Soc.* **146**, 26587-26602, (2024).

21. Wang, Y. *et al.* Highly compressible and environmentally adaptive conductors with high-tortuosity interconnected cellular architecture. *Nat. Synth.* **1**, 975-986, (2022).

22. Wang, J., Wu, B., Wei, P., Sun, S. & Wu, P. Fatigue-free artificial ionic skin toughened by self-healable elastic nanomesh. *Nat. Commun.* **13**, 4411, (2022).
23. Jama, C. *et al.* X-ray photoelectron spectroscopy study of carbon nitride coatings deposited by IR laser ablation in a remote nitrogen plasma atmosphere. *Surf. Interface Anal.* **31**, 815-824, (2001).
24. Briggs, D. & Beamson, G. Primary and secondary oxygen-induced C1s binding energy shifts in x-ray photoelectron spectroscopy of polymers. *Anal. Chem.* **64**, 1729-1736, (1992).
25. Xu, Z. *et al.* Hierarchically aligned heterogeneous core-sheath hydrogels. *Nat. Commun.* **16**, 400, (2025).
26. Yang, Y., Ru, Y., Zhao, T. & Liu, M. Bioinspired multiphase composite gel materials: From controlled micro-phase separation to multiple functionalities. *Chem* **9**, 3113-3137, (2023).
27. Buzin, A. I., Pyda, M., Costanzo, P., Matyjaszewski, K. & Wunderlich, B. Calorimetric study of block-copolymers of poly(n-butyl acrylate) and gradient poly(n-butyl acrylate-co-methyl methacrylate). *Polymer* **43**, 5563-5569, (2002).
28. Wang, X. *et al.* Stretch-Induced Conductivity Enhancement in Highly Conductive and Tough Hydrogels. *Adv. Mater.* **36**, 2313845, (2024).
29. Zhao, C. *et al.* Layered nanocomposites by shear-flow-induced alignment of nanosheets. *Nature* **580**, 210-215, (2020).
30. Zhu, S. *et al.* Bioinspired structural hydrogels with highly ordered hierarchical orientations by flow-induced alignment of nanofibrils. *Nat. Commun.* **15**, 118, (2024).
31. Li, X. *et al.* Effect of mesoscale phase contrast on fatigue-delaying behavior of self-healing hydrogels. *Sci. Adv.* **7**, eabe8210, (2021).
32. Li, M. *et al.* Superstretchable, yet stiff, fatigue-resistant ligament-like elastomers. *Nat. Commun.* **13**, 2279, (2022).
33. Steck, J., Kim, J., Kutsovsky, Y. & Suo, Z. Multiscale stress deconcentration amplifies fatigue resistance of rubber. *Nature* **624**, 303-308, (2023).
34. Narupai, B. *et al.* Simultaneous Preparation of Multiple Polymer Brushes under Ambient Conditions using Microliter Volumes. *Angew. Chem. Int. Ed.* **57**, 13433-13438, (2018).
35. Perry, I. B. *et al.* Direct arylation of strong aliphatic C–H bonds. *Nature* **560**, 70-75, (2018).
36. Xiang, C. *et al.* Stretchable and fatigue-resistant materials. *Mater. Today* **34**, 7-16, (2020).
37. Cooper, C. B. *et al.* Autonomous alignment and healing in multilayer soft electronics using immiscible dynamic polymers. *Science* **380**, 935-941, (2023).
38. Oh, S. *et al.* Organic Dispersion of Mo3Se3– Single-Chain Atomic Crystals Using Surface Modification Methods. *ACS Nano* **16**, 8022-8029, (2022).
39. Kirtane, A. R. *et al.* Development of oil-based gels as versatile drug delivery systems for pediatric applications. *Sci. Adv.* **8**, eabm8478, (2022).
40. Verma, P. *et al.* Visible-Light-Driven Photocatalytic CO2 Reduction to CO/CH4 Using a Metal–Organic "Soft" Coordination Polymer Gel. *Angew. Chem. Int. Ed.* **61**, e202116094, (2022).
41. Wan, H., Wu, B., Hou, L. & Wu, P. Amphibious Polymer Materials with High Strength and Superb Toughness in Various Aquatic and Atmospheric Environments. Adv. Mater. 36, 2307290, (2024).
42. Zhao, R. et al. Ultra-Tough, highly stable and Self-Adhesive Goatskin-Based intelligent Multi-Functional organogel e-skin as Temperature, Humidity, Strain, and bioelectric four-mode sensors for health monitoring. Chem. Eng. J. 485, 149816, (2024).

Methods

Materials

Butyl acrylate (BA, 99.0%), hexyl acrylate (HA, 98.0%), calcium nitrate tetrahydrate ($Ca(NO_3)_2 \cdot 4H_2O$, 98.0%), phosphotungstic acid hydrate ($H_3PW_{12}O_{40} \cdot xH_2O$, PTA, 99.0%), 1-octadecene (90.0%), oleylamine (90.0%), ethanol (99.8%), octane (99.0%), anisole (99.0%), xylene (99.0%), toluene (99.5%), cyclohexene (99.0%), cyclopentene (98.0%), cyclohexane (99.9%), cyclopentane (98.0%), dimethylbutane (99.0%), 1-hexene (99.0%), hexane (97.0%), pentane (99.0%), dodecane (99.0%), isohexane (99.0%), hexadecane (98.0%), 1-(3-dimethylaminopropyl)-3-ethylcarbodiimide hydrochloride (EDC·HCl, 97.0%), dichloromethane (DCM, 99.5%), trifluoroacetic acid (TFA, 99.0%), sodium hydroxide (NaOH, 98.0%), hydrochloric acid (HCL, 37.0%), sodium bicarbonate ($NaHCO_3$, 99.5%), ethylene dimethacrylate (EGDMA, 98.0%), and 2-hydroxy-2-methylpropiophenone (I1173, 98.0%), phenothiazine (98%), RuPhos (95%), RuPhos Pd G1 methyl *t*-butyl ether adduct (95%), sodium tert-butoxide (97%), dioxane (anhydrous, 99.8%), chlorobenzene (anhydrous, 99.8%), were obtained from Shanghai Titan Scientific Co., Ltd., China. 6-Aminocaproic acid (98.0%), 2-hydroxyethyl methacrylate (HEMA, 99.0%), di-*tert*-butyl decarbonate (Boc_2O, 99.0%), and 4-dimethylaminopyridine (DMAP, 99.0%) were purchased from Shanghai Aladdin Scientific Co., Ltd., China. Ethylene bis(2-bromoisobutyrate) (99.0%) was obtained from Adamas. All chemicals were used as received without further purification.

Instrumentation

X-ray photoelectron spectroscopy (XPS) was performed using a Thermo Scientific ESCALAB 250. Fourier-transform infrared (FTIR) spectra were acquired using a Bruker Nicolet IS50 FTIR spectrometer with 32 averaged scans over 4000 to 500 cm^{-1}. Transmission electron microscope (TEM) imaging was conducted using a JEOL JEM-2100F (200 kV). ^1H and ^{13}C nuclear magnetic resonance (NMR) spectra were obtained using Bruker 400 MHz or 500 MHz NMR spectrometers in $CDCl_3$ and referenced to the residual proton in $CDCl_3$ at δ = 7.26 ppm for ^1H and δ = 77.16 ppm for ^{13}C, respectively. Scanning electron microscope (SEM) images were obtained using a HITACHI SU8600. Energy-dispersive X-ray spectroscopy (EDS) elemental mapping results were obtained using a JEOL JEM 2100F (200 KV). UV-vis absorption spectra were obtained using a UV-3600Plus spectrophotometer (Shimadzu). Optical images were captured using an optical microscope (LW300LJT, CEWEI Optoelectronics Technology Co., Ltd., China). Rheological tests were conducted using a TA Instruments ARES-G2 Rheometer at room temperature (26 °C). Circular organogel flakes with the diameter of 8 mm and thickness of 1.5 mm were used for rheological tests. The frequency-dependent sweep was performed range from 0.5 to 100 rad s^{-1} at a constant shear strain of 1%. Small-angle X-ray scattering **(**SAXS) tests were conducted using a Xeuss 3.0 UHR system (XENOCS SAS, France) with an X ray of λ = 1.3414 Å. The sample-to-detector distance was set as 1600 mm, allowing the collection of scattered intensity across a range of scattering vector from 0.001 to 0.36 $Å^{-1}$. The exposure time was 180 s for all SAXS measurements unless otherwise stated.

Synthesis of Boc-6-aminocaproic acid

6-Aminocaproic acid (1.31 g, 1.0 eq) and Boc_2O (2.18 g, 1.0 eq) were dissolved in a mixture of dioxane and deionized water (50 mL, v/v 1:4,) in the presence of NaOH (0.4 g, 1 eq). The mixture was reacted for 12 h at room temperature (26 °C). Then, dioxane was removed with the rotary evaporator, and the aqueous residue was acidified with dilute HCl to pH 4-5. After the product was extracted from the solution with ethyl acetate, the combined organic phase was separated, washed with brine, and dried over anhydrous Na_2SO_4. Finally, the organic phase was concentrated in vacuo to obtain Boc-6-aminocaproic acid as a white solid. Yield: 2.50 g (95%). ^{1}H NMR (500 MHz, $CDCl_3$): δ 4.65 (s, 1H, A = 0.8), 3.16 – 2.94 (m, 2H, A = 2.0), 2.31 (td, J = 7.5, 4.0 Hz, 2H, A = 2.0), 1.62 (dd, J = 9.2, 6.0 Hz, 3H, A = 2.9), 1.53 – 1.39 (m, 11H, A = 10.7), 1.34 (ddd, J = 9.0, 6.6, 3.7 Hz, 2H, A = 2.1). "A" represents the actual relative integral area of the NMR characteristic peak.

Synthesis of Boc-acrylate

Boc-6-aminocaproic acid (1.8 g, 1.0 eq), DMAP (0.095 g, 0.1 eq) and EDC·HCl (2.24 g, 1.5 eq) were dissolved in 20 mL DCM. After cooling in an ice bath, HEMA (1.22 g, 1.2 eq) in DCM (10 mL) was added dropwise. The mixture was stirred at room temperature for 48 h. DCM was removed by rotary evaporation, and the crude product was washed with dilute brine, dried over Na_2SO_4, and concentrated. Purification via flash column chromatography (silica gel, PE/EA = 5:1 v/v) afforded Boc-acrylate as a colorless oil. Yield: 2.18 g (81%). ^{1}H NMR (500 MHz, $CDCl_3$): δ 6.11 (dq, J = 2.0, 1.1 Hz, 1H, A = 1.0), 5.58 (p, J = 1.6 Hz, 1H, A = 1.0), 4.37 – 4.28 (m, 4H, A = 4.1), 3.09 (q, J = 6.7 Hz, 2H, A = 2.0), 2.32 (t, J = 7.5 Hz, 2H, A = 2.0), 1.93 (t, J = 1.3 Hz, 3H, A = 3.0), 1.66 – 1.59 (m, 3H, A = 2.6), 1.42 (s, 9H, A = 9.0), 1.33 (td, J = 7.2, 1.6 Hz, 4H, A = 4.2). "A" represents the actual relative integral area of the NMR characteristic peak.

Synthesis of Amino-acrylate

Boc-acrylate (2.18 g, 1.0 eq) was dissolved in DCM (24 mL), followed by addition of TFA (6 mL). The reaction mixture was stirred at room temperature (26 °C) for 12 h. Volatile components (TFA/DCM) were removed via rotary evaporation under reduced pressure. The residue was dissolved in deionized water (20 mL), neutralized to pH 8.0 with excess $NaHCO_3$ (until gas evolution ceased), and extracted with ethyl acetate (50 mL). The organic layer was dried over anhydrous Na_2SO_4 and concentrated to afford Amino-acrylate as a colorless oil. Yield: 1.31 g (86%). ^{1}H NMR (500 MHz, $CDCl_3$): δ 6.10 (tt, J = 2.3, 1.1 Hz, 1H, A = 1.0), 5.58 (p, J = 1.6 Hz, 1H, A = 1.0), 4.36 – 4.26 (m, 4H, A = 4.0), 2.89 (dd, J = 8.5, 6.7 Hz, 2H, A = 2.0), 2.32 (t, J = 7.3 Hz, 2H, A = 2.0), 1.92 (dt, J = 5.5, 1.3 Hz, 3H, A = 3.0), 1.63 (dt, J = 15.4, 7.8 Hz, 4H, A = 3.6), 1.52 – 1.29 (m, 4H, A = 4.4). "A" represents the actual relative integral area of the NMR characteristic peak.

Synthesis of Ca-POM nanowires without polymerizable ligands (NWs)

The synthesis of NWs using only oleylamine as the ligand followed an established procedure[17]. In a typical experiment, $H_3PW_{12}O_{40}\cdot xH_2O$ (1.00 g, 0.347 mmol) and $Ca(NO_3)_2\cdot 4H_2O$ (0.123 g, 0.520 mmol) were dissolved in 16 mL deionized water, yielding a clear aqueous solution.

After stirring for 10 min, 1-octadecene (12 mL) and oleylamine (4 mL, 9.7 mmol) were sequentially added. The mixture was stirred for 8 h at room temperature (26 °C), during which marked viscosity increase occurred. The product was subjected to three ethanol/octane wash-centrifugation cycles to yield NWs with the centrifugation condition of 2000 × g.

Synthesis of Ca-POM nanowires with polymerizable ligands (PNWs)

The synthesis of PNWs closely followed the synthesis protocol established for Ca-POM NWs in prior methodology. In a typical experiment, $H_3PW_{12}O_{40}\cdot xH_2O$ (1.00 g, 0.347 mmol) and $Ca(NO_3)_2\cdot 4H_2O$ (0.123 g, 0.520 mmol) were dissolved in 16 mL deionized water, yielding a clear aqueous solution. After stirring for 10 min, 1-octadecene (12 mL), oleylamine (4 mL, 9.7 mmol), and a predetermined amount of polymerizable ligand (Amino-Acrylate, 1.6 mmol for the standard 6:1 oleylamine-to-polymerizable ligand ratio) were sequentially added. The mixture was stirred for 8 h at room temperature (26 °C), during which marked viscosity increase occurred. The product was subjected to three ethanol/octane wash-centrifugation cycles to yield PNWs with the centrifugation condition of 2000 × g.

For PNWs with different oleylamine-to-polymerizable ligand ratios, the synthetic procedure was identical except for varying the quantity of the added polymerizable ligand. For PNW samples with 5:2 and 12:1 oleylamine-to-polymerizable ligand ratios, the added amounts of the polymerizable ligand were 3.9 mmol and 0.8 mmol, respectively. These PNW variants with 5:2 and 12:1 oleylamine-to-polymerizable ligand ratios were termed as PNW_h and PNW_l, respectively (see Table S2 for details). Unless otherwise stated, all the PNW referenced in this work refers to the formulation of 6:1 oleylamine-to-polymerizable ligand ratio.

Synthesis of PTH photosensitizer

A 100 mL two-necked round-bottom flask was fitted with a magnetic stir bar, a reflux condenser, an argon inlet, and a rubber septum. To this flask were added sodium tert-butoxide (NaOtBu, 2.09 g, 17.5 mmol), phenothiazine (2.50 g, 12.5 mmol), RuPhos precatalyst (103 mg, 0.21 mmol, 1.7 mol%), and RuPhos ligand (100 mg, 0.21 mmol, 1.7 mol%). The flask was evacuated and backfilled with argon three times to thoroughly remove air and moisture. Under argon, anhydrous 1,4-dioxane (12.5 mL) and anhydrous chlorobenzene (2.00 mL, 17.6 mmol) were added via syringe. The resulting mixture was heated to 110 °C with vigorous stirring and maintained at this temperature for 5 hours, during which a gradual color change was observed. After cooling to room temperature, the reaction mixture was quenched and diluted with dichloromethane (40 mL). It was then transferred to a separatory funnel and washed sequentially with water and brine to remove inorganic salts. The organic layer was separated, dried over anhydrous magnesium sulfate ($MgSO_4$), and filtered to remove the desiccant. The filtrate was concentrated under reduced pressure using a rotary evaporator to yield a crude solid. The crude product was purified by flash column chromatography on silica gel (eluent: 95:5 hexanes/ethyl acetate). The purified product, 10-phenylphenothiazine, was obtained as a pale-yellow crystalline solid (3.12 g, 94% yield). The corresponding reaction equation and full NMR spectra are available in the Supplementary Information, Fig. S7. ^{1}H NMR (500 MHz, $CDCl_3$): δ 7.64 (t, J = 7.7 Hz, 2H),

7.57 – 7.49 (m, 1H), 7.48 – 7.38 (m, 2H), 7.08 (dd, *J* = 7.0, 2.1 Hz, 2H), 6.88 (pd, *J* = 7.3, 1.7 Hz, 4H), 6.27 (dd, *J* = 7.7, 1.8 Hz, 2H).

Preparation of physically crosslinked NW and PNW organogels

The NW-octane and PNW-octane organogels were prepared following an established procedure[17]. First, NWs or PNWs were dispersed in octane at a concentration of approximately 10.0 wt%. The dispersion was centrifuged at 2000 rpm to remove bubbles. After standing for several hours at room temperature (26 °C), the physically crosslinked NW-octane or PNW-octane organogels was obtained. Notably, PNWs modified with the polymerizable ligand retained the capability to form stable physical organogels in octane, implying that the incorporation of the polymerizable ligand does not disrupt nanowire network formation in octane. Moreover, both NWs and PNWs were dispersed in a 1:1 (w/w) BA/octane mixture to form physically crosslinked organogels, which were designated as the NW-BA-octane and PNW-BA-octane organogels, respectively. These physical organogels formed in BA/octane mixtures, with the addition of a photosensitizer and a photoinitiator, were employed as the precursor for the preparation of NW-PBA-octane and PNW-PBA-octane organogels (see below for details).

Preparation of PNW-PBA organogels

The PNW-PBA organogels were synthesized from the precursor PNW-BA-octane physical organogels described in the aforementioned discussion. Take the PNW7-PBA46 organogel (see Table S1 for details) as the example, in a typical experiment, the precursor physical organogel was prepared by dispersing PNW (0.35 g) in octane (2.35 g), followed by the addition of BA (2.30 g), PTH photosensitizer (5 mg), and initiator (6.6 mg). The mixture was thoroughly vibrated and then centrifuged at 2000 rpm for 10 min to remove air bubbles, forming a physically crosslinked PNW-BA-octane organogel precursor. The precursor was then carefully transferred into a custom-made mold (40 × 40 × 2 mm^3 in dimension) and UV-cured (365 nm UV light, 36 W) for 2 h. After photo-initiated polymerization, the resulting PNW7-PBA46 organogel was removed from the mold and cut into specific shape for further testing. Other PNW-PBA organogels with different compositions can be similarly prepared by adjusting the component ratios or using different PNWs (SupplementaryTable 1-3). Moreover, a control experiment (discussed in the Supplementary Note 1) photo-initiated the precursor PNW-BA-octane physical organogel and exhibited lower photo-initiation efficiency. This phenomenon may be associated with the well-documented photocatalytic activity of tungsten-containing POM clusters[34,35].

Preparation of PNW-PHA organogels

The synthetic procedure of PNW-PHA organogels was identical to that of the PNW-PBA organogels, except that the BA monomer was replaced with HA monomer.

Preparation of NW-PBA organogels

The NW-PBA organogels were fabricated analogously to the procedure of the PNW-PBA organogels, except that the PNW was replaced with NW.

Preparation of PBA organogels

A precursor solution was prepared by mixing BA (2.30 g), octane (2.35 g), crosslinker EGDMA (4 mg), and photoinitiator I1173 (3 mg). The precursor solution was then transferred into a custom-made mold ($40 \times 40 \times 2$ mm^3 in dimension) and UV-cured (365 nm UV light, 36 W) for 2 h. After photo-initiated polymerization, the obtained PBA organogel was removed from the mold and cut into specific shape for further testing.

Mechanical tests

The mechanical properties of organogels under tension and compression were characterized using a universal testing machine (Instron 5965) equipped with a 100 N load cell. For compression testing, cylindrical samples (8 mm diameter × 1.5 mm thickness) were used. Dumbbell-shaped specimens ($20 \times 2 \times 1.5$ mm^3) were employed for tensile testing. The strain rates of the tensile and compression tests were 100 mm min^{-1} and 5 mm min^{-1}, respectively, at a predetermined strain. Cyclic loading tests were performed at identical strain rates with predetermined strain levels. True stress, calculated by multiplying nominal stress by the deformation ratio under the incompressibility assumption, was used to account for dimensional changes during deformation. Tensile toughness was determined by integrating the area under the nominal stress-strain curve up to fracture. The fracture energy Γ was calculated using single-edge notch tension (SENT) tests[6,33,36], as discussed in the Supplementary Note.

Self-healing of the PNW7-PBA46 organogel

Self-healing capability was assessed by cutting dumbbell-shaped PNW7-PBA46 organogel strips ($20 \times 2 \times 1.5$ mm^3 in size) into two halves and then bringing the fractured surfaces into direct conformal contact[37]. The organogel samples were allowed to heal for 24 h under ambient conditions, after which the mechanical properties were evaluated utilizing an Instron 5965 instrument, at a constant strain rate of 100 mm min^{-1} with a 100 N load cell. Optical images of the healed sections were captured using a transflective optical microscope (LW300LJT). The self-healing experiment was repeated with three independent samples under identical conditions.

Freeze-thaw treatment to the PNW7-PBA46 organogel

A square PNW7-PBA46 organogel sample ($20 \times 20 \times 1.5$ mm^3 in size) was completely immersed in liquid nitrogen for more than 10 min. After removal from liquid nitrogen, the organogel was allowed to naturally warm to room temperature. Although the organogel network lost its elasticity upon freezing in liquid nitrogen, no structural damage was observed. As the temperature gradually returned to ambient conditions, the organogel recovered its elasticity. Subsequently, the mechanical properties were characterized using a universal test machine (Instron 5965) to assess cryogenic stability.

Organic liquid absorption by the PNW7-PBA46 organogel

Dried PNW7-PBA46 organogels (8 mm diameter × 1.5 mm height), prepared via ambient air-drying for 72 h, were immersed in excess nonpolar solvents, including octane, anisole, xylene, toluene, cyclohexene, cyclopentene, cyclohexane, cyclopentane, dimethylbutane, 1-hexene, hexane, pentane, dodecane, isohexane, and hexadecane. Absorption capacity was quantified by monitoring mass gain relative to the initial dry mass over time. The quantity of organic solvent was maintained in substantial excess (over 1000 times) compared to the initial dried organogel mass to ensure saturation absorption. Identical protocols were applied for the organic liquid absorption experiments of PNW-PHA and PBA organogels.

Oil spill recovery experiment

In a typical experiment, 12 mL petrol (commercial #92 petrol in China) was poured into a beaker. Then a piece of dried PNW7-PBA46 organogel (0.4 g) was added into the petrol. The absorption of petrol by the organogel reached equilibrium in about 8 h. The swollen PNW-BA-petrol organogel, retained mechanically self-standing and structural integrity for direct transfer to a rotary evaporator. Vacuum distillation using the rotary evaporator recovered the absorbed petrol and the piece of dried organogel in the initial state. The process can be repeated at least 10 times and no obvious decrease in the absorption capability of petrol was observed during the consecutive 10 repetitions.

Summary of Key Properties in Representative Nonpolar Organogels

The Supplementary Table 4 compiles and compares several key properties of representative nonpolar organogels reported in recent literature[38-40], and the Supplementary Table 5 compares several key properties of our work with representative polar organogels reported in recent literature[10,11,41,42].

Acknowledgments

This work was supported by the National Natural Science Foundation of China (22401045 of J.P., 22471079 of K.Y., 22301037 of Z.H., 22241502, 22588301 and 92461314 of X.W.), the Beijing National Laboratory for Molecular Sciences (BNLMS202307) of K.Y., the Science and Technology Program of Guangzhou (2024D03J0003) of K.Y., and the Pearl River Talents Scheme (2016ZT06C322) of K.Y.. We acknowledge Senior Experimental Engineer Dr. Jie Cui from the Analytical and Testing Center of South China University of Technology for the high-angle annular dark-field (HAADF) imaging via transmission electron microscopy (TEM).

Contributions

K.Y. and X.W. conceived the idea and supervised the research. Z.H. and J.P. carried out the experiments. Z.H., J.P., W.Z., K.Y., and X.W. analyzed the data, wrote the draft and revised the manuscript.

Competing interests

The authors declare no competing interests.

Editorial Summary

Although having potentially useful applications, development of organogels that absorb nonpolar liquids is challenging. Here, the authors report the development of organogels with a nanowire-polymer networks, capable of absorbing and gelating nonpolar organic liquids.

Peer review information: *Nature Communications* thanks Jui-Hsiang Liu, and the other, anonymous, reviewer for their contribution to the peer review of this work. A peer review file is available.